Numerical Analysis of the Thermal Resistance of a Multi-Layer Reflective Insulation Material Enclosed by Cavities under Varied Angles

R.S. Pelzers[1], A.W.M. van Schijndel*[2]
[1]Former student Building Physics, [2]Chair Building Physics, Eindhoven University of Technology
*Corresponding author: Eindhoven University of Technology, P.O. Box 513, 5600 MB Eindhoven, The Netherlands, a.w.m.v.schijndel@bwk.tue.nl

Abstract:
This work presents a numerical analysis on the thermal performance of a sample, consisting of two cavities surrounding a Multi-Layer Reflective Insulation (MLRI) material, under various angles and for downward and upward heat flows. It was demonstrated that the sample can reach high thermal resistance values when placed (nearly) horizontal under an upward heat flux, while at different angles and heat flux directions the thermal resistance was substantially lower. The heat transfer by radiation in both cavities is greatly reduced by the highly reflective surfaces of the MLRI material. Meanwhile, convective heat transfer gained a more dominant role on the heat transfer through the sample, since the radiative heat transfer in the cavities is highly decreased. For practical application, MLRI materials are probably best placed in the floor beneath a building so that the highest thermal resistance is attained, since convective heat transfer is minimized due to the upward heat flow.

Keywords: Multi-Layer Reflective Insulation Material, Cavity, CFD, Heat Transfer, Façade

1. Introduction

In the current building industry, several manufactures of insulation materials offer customers Multi-Layer Reflective Insulation (MLRI) materials as an alternative to more commonly used insulation materials. MLRI materials are composed out of multiple layers of diverse materials, depending per type and manufacturer. While commonly-used insulation materials try to minimize thermal conduction, MLRI materials also minimize thermal radiation by using surrounding cavities. Therefore, common insulation materials do not require a cavity to function properly, while MLRI materials need to be adjacent to one of two cavities for maximum thermal resistance. Since the outer layers of the MLRI material have an low emission coefficient, the radiative heat transfer in the surrounding cavities can be reduced up to 97%. An example of MLRI material is illustrated in Figure 1.

Figure 1: An example of a MLRI material.

Conversely, several manufactures claimed that their MLRI product may have extremely high thermal resistance when it is correctly applied in a building components, including facades and roofs. Meanwhile, the MLRI materials are applied on a large scale in the sloping roofs of domestic houses to reduce the heating costs. In the current standards, such as the ISO 6946: 2007 [1], calculation rules are only provided for a cavity adjacent to a reflecting layer in the horizontal or vertical position are provided. Since there is no comprehensive standard in which additional angles are considered, there is uncertainty about the thermal performance of MLRI materials under additional angles for different heat flow directions.
In this article, the claim on a manufactured MLRI material (see Figure 1) is investigated with numerical simulation, using COMSOL 4.2a, and is compared with heat flow measurements of the material. However, first, a literature review of cavities and related work is provided.

2. Theory

2.1 Literature review

The thermal resistance of a building component in which MLRI material is processed is raised by

a conventional cavity adjacent to the MLRI material. Conventional cavities can be subdivided into open and closed cavities and have often a characteristic width of 0.04 m. However, on occasion this value differs, ranging between 0.02-0.05 m. Air velocities in facades with an open cavity range between 0-0.25 m s^{-1} dependent on pressure differences over the cavity, but in vertically-vented cavities may reach up to 0.7 m s^{-1} [2, 3, 4]. The air in open cavities can exhibit higher velocities than air in closed cavities up to four times higher [4]. Also, air velocities in the summer can be slightly higher due higher temperature, generated by higher solar radiation [4]. The pressure differences over a cavity create air flow through the cavity and can be created by local temperature differences or under/overpressures around the building created by wind.

In comparable work [5] measured that the effect of highly-reflective foils in cavities of sloped roofs in-situ and in the laboratorial scale reduced the heat flux, but this effect is affected by convection. In fact, it was found that the heat flux at the top of the roofs was higher than at the bottom of the roofs due to convection.

In another work [6], the heat transfer coefficients for horizontal cavities with different thicknesses were estimated, according to ISO 15099:2003. In several cases reflective material were applied. The study demonstrated that the convective heat transfer increased while the radiative heat transfer decreased. Still, the overall heat transfer coefficient for the ordinary cavities, with a width larger than 20 mm, was estimated around 5.4 W m^{-2} K^{-1}, whereas the cavities with reflective material were estimated lower at 1.8 W m^{-2} K^{-1}.

2.2 Heat flow measurement setup

In Figure 2a, the sample used in the measurements is illustrated, consisting of the MLRI material surrounded by the two cavities.

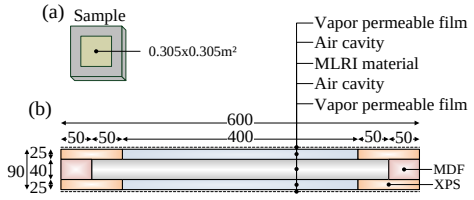

Figure 2: (a) A schematic cross-section of the sample; (b) The monitoring region on the sample.

A heat flux measurement device (heat flux meter) was used for measuring the thermal conductivity of the sample. During the measurements, the sample was measured in the monitoring region illustrated in Figure 2b. The cavities were sealed with a vapor permeable film to ensure that, before measuring, the sample could dehydrate. The edges of the sample were sealed with medium-density fiber board (MDF) and extruded polystyrene (XPS). The heat flux meter is composed out of two plates between which the sample was placed. In the middle of the sample, within an area of 305x305 mm^2, the heat flux is measured with numerous thermocouples. Furthermore, the distance between the plates is measured and fixed at 90 mm. Temperature difference between the plates is regulated with Peltier elements that absorb and release heat to a water flow cooled heat sink system in the device. The edges of the sample are insulated by the heat flow meter to minimize heat transfer. After a series of heat flux measurements, the heat conductivity of a sample was obtained using Fourier's law. For comparison with the simulations of the COMSOL model, the conductivity was obtained for various angles , while applying either an upward or downward heat flux on the sample, as illustrated in Figure 3.

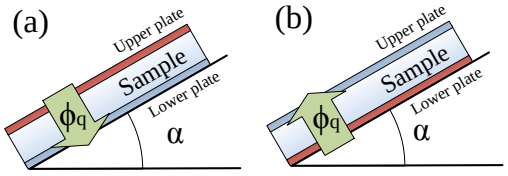

Figure 3: In the setup, the heat flux ($\boldsymbol{\phi_q}$) was directed (a) downwards and (b) upwards at an angle $\boldsymbol{\alpha}$.

2.3 Classification of flow

The flow in the sample (see Figure 2) is identified with two dimensionless parameters to determine the required modules in COMSOL. First of all, the geometry of both cavities is classified, using the height (H [m]) and width (W [m]), to define the aspect ratio (A [-]), computed by [7]:

$$A = \frac{H}{W} \qquad (1)$$

For an α of 90º it is found that A = 16, while for an α of 0º it is found that A = 0.0625. Additionally, the Rayleigh number (Ra [-]) is considered and is defined as [7]:

$$Ra = \frac{{\rho_{air}}^2 g c_{air} \beta (\Delta T) H}{k_{air} \mu_{air}} \quad (1)$$

Where ρ_{air} [kg m^{-3}] is the air density (= 1.246 kg m^{-3} at 283.15 K, 101325 Pa); g [m s^{-2}] the gravitational acceleration (= 9.81 m s^{-2}); c_{air} [J kg^{-1} K^{-1}] is the specific heat capacity of air (= 1.005 J kg^{-1} K^{-1}); β [K^{-1}] is the volumetric coefficient of thermal expansion (= 3.43·10^{-3} K^{-1}) ; k_{air} [W m^{-1} K^{-1}] is the thermal conductivity of air (= 0.025 W m^{-1} K^{-1}); μ_{air} [kg m^{-1} s^{-1}] is the dynamic viscosity of air (= 1.7·10^{-5} kg m^{-1} s^{-1}). The Rayleigh number characterizes the transition between a flow in which conduction or convection is dominant [7].
The Rayleigh numbers for various ΔT and H is computed and illustrated in Table 1, as extreme height occur at respectively α = 0° and α = 90° and various ΔT still undefined.

Table 1: The Rayleigh numbers for various estimated ΔT and extreme H.

		ΔT [K]		
		2	4	6
H [m]	0.025	6,783	13,566	20,348
	0.4	108,524	217,049	325,573

Furthermore, the Prandlt number (Pr [-]) can be applied to determine the ratio between viscous and thermal diffusion (for air Pr = 0.71) [7], but is not considered in this study.
Following the categorization of [8], it is expected that based on the obtained values for Ra and H, steady multicellular motion, fully developed boundary layers, and interacting boundary layers will occur within the simulations of the model, for certain α.
During simulation, multicellular motion may become unsteady, which prevent convergence [9]. This numerical instability typically occurs in the solution when the convection term is larger relative to the diffusion term. If unsteady multicellular solutions occur, an artificial diffusion term could be added to the model to possible stabilize the solutions. As a result, iteration times are decreased and possible required mesh refinement is eliminated. In the current COMSOL simulation, both a streamline and crosswind diffusion (on by default) and isotropic diffusion (off by default) are applied in accordance with [7].

2.4 Analytical calculation

To aid the identification of the heat transfer coefficients of the heat transfer mechanisms in the cavities, an analytical calculation was created. The analytical calculation is derived from a thermal circuit representing the sample, as illustrated in Figure 4. In the calculation, the heat transfer coefficients are averaged over the two cavities. Furthermore, all values are considered in the middle of the sample over an area of 0.305x0.305 m2, the monitoring region (see Figure 2b).

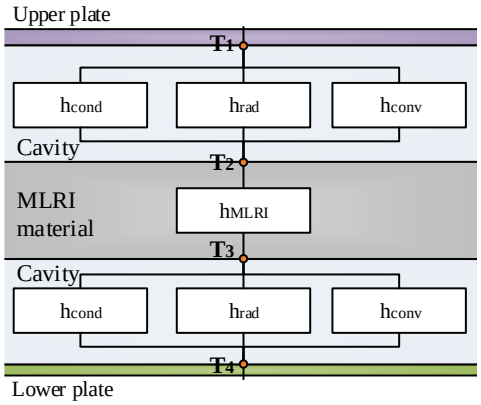

Figure 4: An abstract representation of the setup in the form of a thermal circuit. The thermal resistance between the nodes is expressed by heat transfer coefficients.

First, the heat flux (ϕ_q [W m^{-2}]) through the sample is computed by:

$$\phi_q = U_s(\Delta T) \quad (1)$$

Where U_s [W m^{-2} K^{-1}] is the thermal conductance of the sample; ΔT [K] is the temperature difference over the sample ($\Delta T = T_1 - T_4$). In the circuit, the heat transfer coefficient of the sample is further composed by h_{MLRI} and h_c [W m^{-2} K^{-1}], the heat transfer coefficients of respectively the MLRI material and a cavity, and are related by:

$$\frac{1}{U_s} = \frac{1}{h_{MLRI}} + \frac{1}{2h_c} \quad (2)$$

The heat transfer coefficient of a cavity is further defined by:

$$h_c = h_{cond} + h_{rad} + h_{conv} \quad (3)$$

Where h_{cond}, h_{rad} and h_{conv} are the heat transfer coefficients created by respectively conduction, radiation and convection.
Conduction can be computed using:

$$h_{cond} = \frac{k_{air}}{d_{cav}} \quad (4)$$

Where k_{air} [W m^{-1} K^{-1}] is the average thermal conductivity of air in the cavities; and d_{cav} [m] is the depth of a cavity. The average thermal conductivity of air can be derived from the numerical model. Consecutively, the heat transfer coefficient of radiation can be computed with:

$$h_{rad} = -\frac{\bar{q}_{rad}}{\Delta T_c} \quad (5)$$

Where $\bar{q}_{rad}$ [W m^{-2}] the average radiative heat flux in the cavities within the monitoring region; and ΔT_c [K] is the average temperature difference in the cavities within the monitoring region, computed according to:

$$\Delta T_c = (T_1 - T_2 + T_3 - T_4)/2 \quad (6)$$

Finally, h_{conv} can be computed by combining and rewriting equations (1) - (6).

3. Model definition

3.1 Method

In Section 2.3 was found that steady multicellular motion, fully developed boundary layers, and interacting boundary layers may occur during simulation, dependent on the temperature differences and applied angle. Therefore, no turbulent flow is expected (see [8]). Hence, no turbulent model is applied. Following the model "*Buoyance Flow in Free Fluids*" from the COMSOL model gallery [10], the incompressible Navier-Stokes equations are applied with a Boussinesq buoyance term included to account for the thermal-induced convection in the cavities. The Heat Tranfser (*ht*) and Laminar Flow module (*spf*) are selected for the modeling. The simulations are conducted using a time dependent iteration with a range of 0 – 50000, with monitoring steps of 100 to limit the file size. The flow was stabilized with streamline, crosswind and isotropic diffusion, using the found values of [7]. Therefore, the turning parameters C_k [-] and δ_{id} [-] for the stabilization were set to respectively 0.1 and 0.15. The radiation was simulated in COMSOL with the surface-to-surface radiation option.

3.2 Geometry

For the model geometry, the dimensions in Figure 2 of the sample was adapted. In addition, both the upper and lower plate were modeled with a stretching out over the whole length of the sample with both a height of 1 mm. Therefore, the dimensions of the outer edges of the model are 600 mm x 92 mm (length x height).

3.3 Governing equations

In the Laminar Flow module, the Navier Stokes equations for an incompressible flow a time-dependent system are defined for air as:

$$\rho_{air}\frac{\partial u}{\partial t} + \rho_{air}(u \cdot \nabla)u = -p\nabla + \nabla \cdot \mu(\nabla u + (\nabla u)^T) + F_g \quad (7)$$

$$\frac{\partial \rho_{air}}{\partial t} + \nabla \cdot u\rho_{air} = 0 \quad (8)$$

Where u [m s^{-1}] is the velocity vector; t [s] is time; p [Pa] is pressure; and F_g [kg m^{-2} s^{-2}] is the gravitational term. Furthermore, the heat transfer equations in the Heat Transfer module for a material n are defined by:

$$\rho_n c_n \frac{\partial T}{\partial t} + \nabla \cdot (-k_n \nabla T) = -\rho_n c_n u \cdot \nabla T \quad (9)$$

Where ρ_n [kg m^{-3}] is the density; c_n [J kg^{-1} K^{-1}] is the specific heat capacity; and k_n [W m^{-1} K^{-1}] is the conductivity of air. The gravitational term is further defined as:

$$F = \begin{bmatrix} x \\ y \end{bmatrix}$$
$$x = -\rho_{air} \cdot g \cdot \sin\alpha \quad (10)$$
$$y = -\rho_{air} \cdot g \cdot \cos\alpha$$

Where ρ_{air} [kg m^{-3}] is the density of air; g [m s^{-2}] the gravitational acceleration (= 9.81 m s^{-2}); and α [-] is the angle of the sample. The relation between angle of the sample and direction of F_g is illustrated in Figure 5.

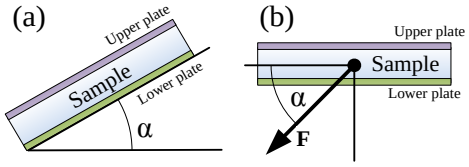

Figure 5: (a) The angle of the sample; (b) The angle of the sample translated to F.

ρ_{air} is further defined, as the Boussinesq approximation is applied and air is considered as an ideal gas, by:

$$\rho_{air} = \rho_{ref}\beta_p(T_{air} - T_{ref}) \quad (11)$$

Where β_p [K^{-1}] is the volumetric thermal expansion coefficient for an ideal gas (= $1/T_{STP} \approx 3.7\cdot10^{-3}$ K^{-1} [11]); ρ_{ref} [kg m^{-3}] is the reference density for the reference temperature (T_{ref} [K]). For air at 273.15 K and 103,124 Pa, ρ_{ref} = 1.293 kg m^{-3} [11]. Now, the laminair flow and the heat tranfer interfaces are 2-way coupled through the transport of heat by fluid velocity and fluid movement initiated through density differences due to temperature.

3.4 Initial and boundary conditions and material properties

All materials are modeled isotropic. Furthermore, the gravitational constant was set to 9.81 m s^{-2} and α was set to the corresponding angle of the simulation, varying between 0° and 90° with an interval of 15°. An overview of the boundary conditions are presented in Figure 6 for which the boundary values are found in Table 2. Moreover, the initial conditions in Table 3 and the main properties of the materials in Table 4. In addition, the dynamic viscosity of $1.7\cdot10^{-5}$ Pa s for the air is selected for computation of the air flow. Also, it should be remarked that the heat resistance of the plates (see Section 3.2) is $2\cdot10^{-5}$ m^2 K W^{-1} and can therefore be ignored.

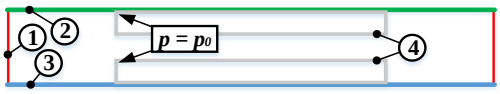

Figure 6: The boundary conditions in the model: (1) thermal insulation; (2) temperature, T_u [K]; (3) temperature, T_l [K] (4) no slip. Two pressure point constrains are made in the model where $p = p_0$.

Table 2: Boundary values.

Parameter	Value	Unit
T_u	273.15 or 293.15	K
T_l	293.15 or 273.15	K

Table 3: Initial conditions.

Parameter	Value	Unit
p_0	101,300	Pa
T_0	283.15	K
u_0	0	m s^{-1}

Table 4: The main material properties.

		Parameter			
		k_n [W m^{-1} K^{-1}]	c_n [J kg^{-1} K^{-1}]	ρ_n [Kg m^{-3}]	ε_n [-]
Material	XPS	0.03	1,470	20	0.9
	MDF	0.08	2,100	300	0.9
	edge	99	10	10	0.9
	MLRI	0.0284	1,355	87	0.03
	Air	0.025	1,005	*	-

*** Computed using equation 11**

3.5 Grid generation and convergence check

During this modeling study, the grid error was not defined. Still, the structured mesh was applied, as exemplified in Figure 7. The cells near the boundary are smaller in order to promote correct computation of the boundary layers. The cell quality was considered by limiting the size ratio of adjacent cells to 20%.

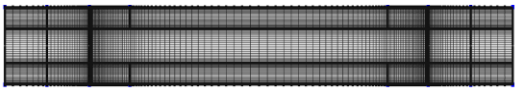

Figure 7: The structured grid of the model, consisting of 13,746 quadrilateral cells.

The converge of the model was checked by considering the residual RMS error as is was reduced to an acceptable value (usually 10^{-4}), monitoring the temperature to have reached a steady solution within the monitoring region (a 305 mm area centered in the middle of the sample, similar to the sensor locations of the heat flow device) and checking if the system had an heat flow imbalances between the lower and upper plate is less than 1% (= steady state).

4. Results and discussion

4.1 Validation and flow field evaluation

The model was simulated for the different angles for both the upward and downward heat flux and was compared with the measurements in Figure 8. With exception of the angles 0, 15 and 30 with an upward heat flow, the modeling error exceeds the 5%. A closer investigation of the velocity magnitude field, illustrated in Figure 9, reveals the origin of the modeling error. The transitional regime between steady multicellular motion and interacting boundary layers and interacting boundary layers seems to introduce an considerable error in the heat resistance calculation. The vertical convective heat transport is underestimated. Despite the large modeling errors, the simulation and measurements show similar trends.

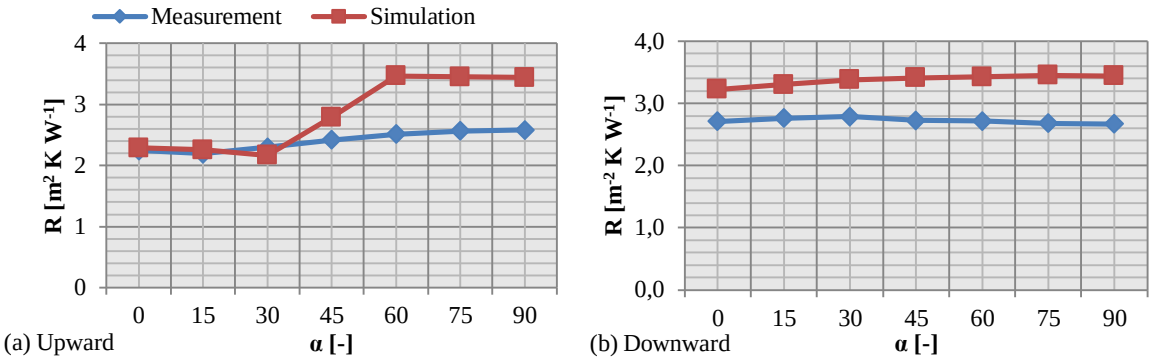

Figure 8: The heat resistance per angle for the (a) upward heat flux and (b) downward heat flux.

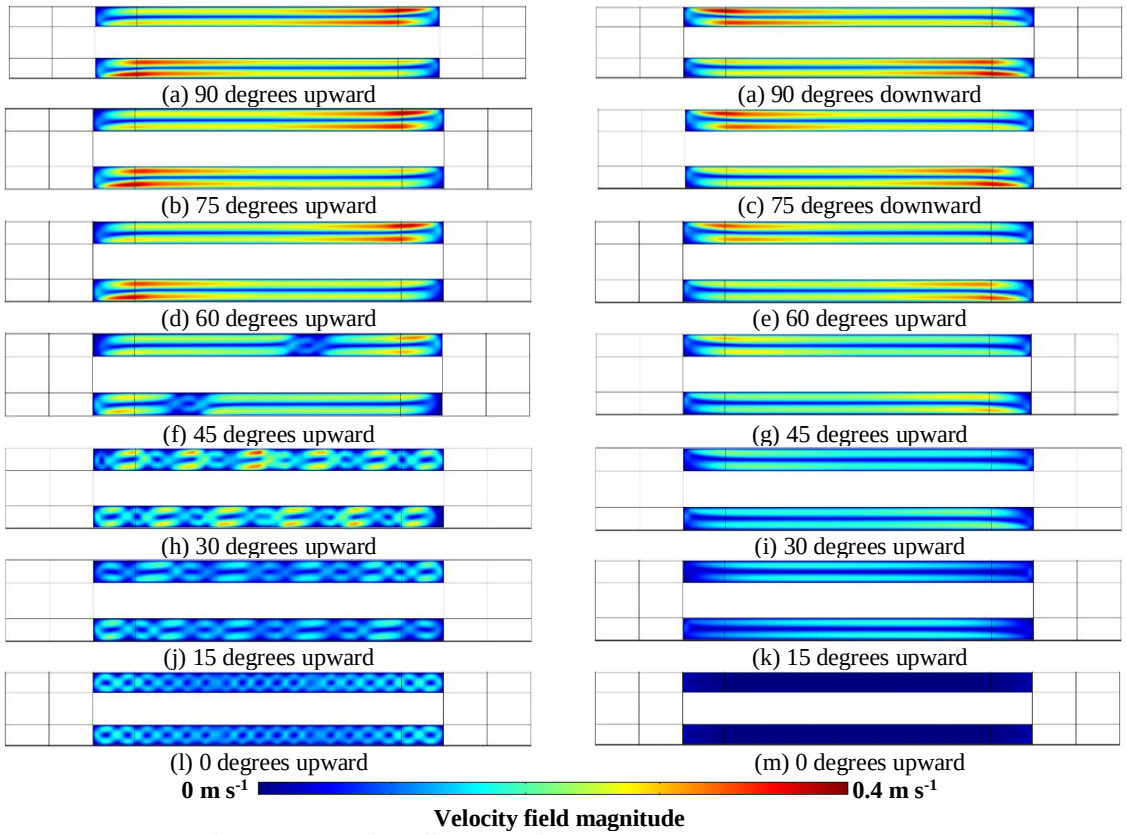

Figure 9: The velocity field magnitude for different heat flux directions and angles.

4.3 Different emission values for the MLRI material

In line with [6], the cavities surrounding the MLRI material are considered for an regular and highly reflective surfaces emission coefficient as ε_{MLRI}. In Figure 10 the heat transfer coefficients for the three heat transfer mechanisms at different angles and heat flux directions are reported. The equations of Section 2.4 were applied analytically derive the data in Figure 10. Clearly, for conventional cavities, radiation is the dominant heat transfer mechanism. However, when the radiation is reduced by a highly reflective surface, convection becomes the dominant heat transfer mechanism which makes the heat resistance highly dependent on the angle of the sample.

The average overall heat transfer coefficient for ε_{MLRI} = 0.9 is 5.5 W m^{-2} K^{-1} which is comparable with the 5.4 W m^{-2} K^{-1} found in [6]. Meanwhile, the cavities with reflective material (ε = 0.05) were estimated around 1.8 W m^{-2} K^{-1} by [6], but average overall heat transfer coefficient for ε_{MLRI} = 0.03 is 2.5 W m^{-2} K^{-1}. This suggest that the heat transfer by convection is not well estimated.

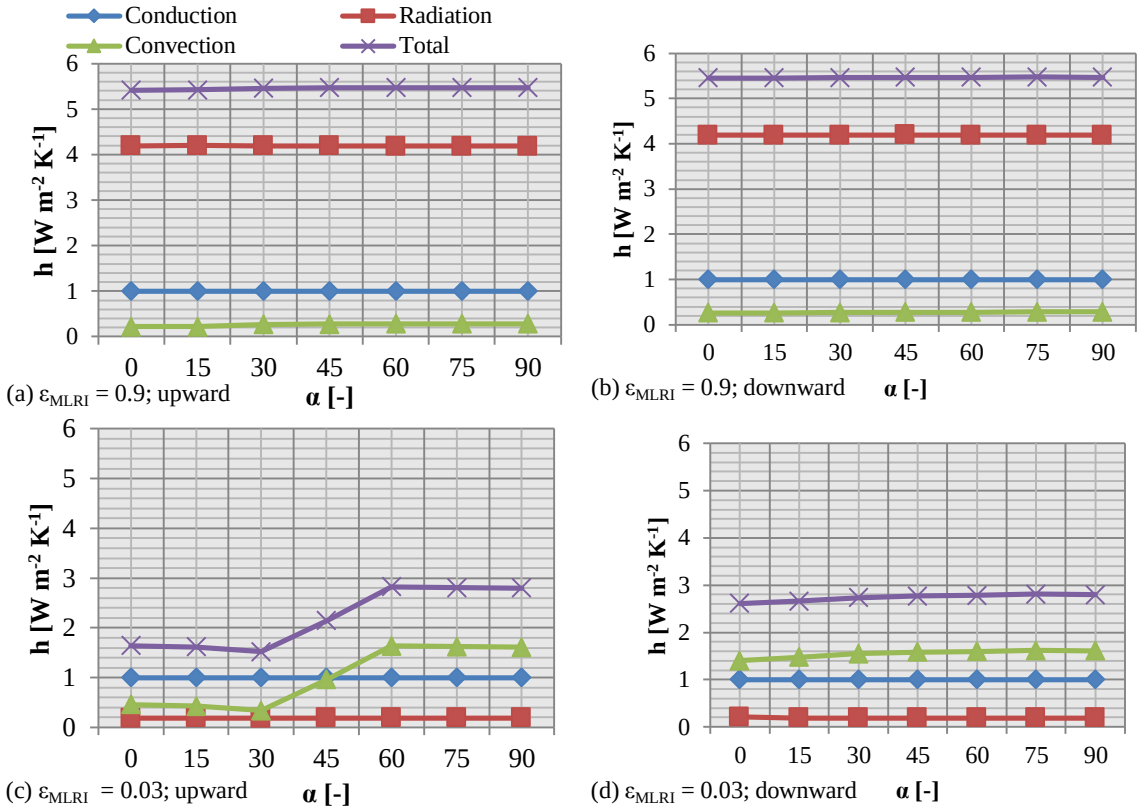

Figure 10: The heat transfer coefficient for each heat transfer mechanism and the total heat transfer per angle for the upward heat flux and downward heat flux for an $\boldsymbol{\varepsilon_{MLRI}}$ of respectively (a & b) 0.9 and (c & d) 0.03.

5. Conclusions

During this numerical study it was found that with the current modeling approach the heat flux measurements of the sample could only be reproduced with significant error. Closer observation revealed that the convective component was the source of a large deviation between the measurements and the numerically-obtained results. Nonetheless, the numerical model did show similar trends as the experimental results and the overall heat transfer coefficient of the cavities exhibited similarities with other computed results from literature. Furthermore, by applying an analytical post-computation, the numerical results could provide more detailed information about the contribution of the individual heat transfer mechanisms in

relation to each other. For example, it was found that the effects of radiative heat transfer in the cavities, while applying ordinary emission coefficient to the MLRI material (ε_{MLRI} = 0.9), is dominant. In contrast, when a low emission coefficient is applied to the MLRI material (ε_{MLRI} = 0.03), convective heat transfer is dominant, with exception from simulation in which an downward heat flow and a tilt of 45° or less. In fact, simulation show, in agreement with measurements (error = 2%), that convective heat transfer for an downward heat flow at a tilt of 0° is minimalized to 28% of the total heat transfer. Therefore, the highest heat resistance values are obtained when MLRI materials are applied in a buildings component in which mainly upward flow occurs. For example, the ground floor rather than the (sloped) roof of a building. Still, the current numerical modeling of convection in the cavities should be developed further, since considerable modeling errors were found.

6. References

[1] I. O. f. Standardization, ISO 6946:2007: Building components and building elements - Thermal resistance and thermal transmittance - Calculation method, 2007.

[2] J. Falk and K. Sandin, "Ventilated rainscreen cladding: Measurements of cavity air velocities, estimation of air change rates and evaluation of driving forces," *Building and Environment*, **no. 59**, pp. 164-176, 2012.

[3] C. Sanjuan, M. Sánchez, M. Heras and E. Blanco, "Experimental analysis of natural convection in open joint ventilated façades with 2D PIV," *Building and Environment*, **no. 46**, pp. 2314-2325, 2011.

[4] C. Sanjuan, M. Suárez, M. González, J. Pistono and E. Blanco, "Energy performance of an open-join ventilation façade compared with a conventional sealed cavity façade," *Solar Energy*, **no. 85**, pp. 1851-1863, 2011.

[5] S. Roels and M. Deurinck, "The effect of a reflective underlay on the global thermal behaviour of pitched roofs," *Buildng and Environment*, **no. 46**, pp. 134-143, 2011.

[6] S. Uvslokk and H. Arnesen, "Thermal insulation performance of reflective material layers in well insulated timber frame structures," *Proceedings of the 8th Symposium of building physics in the Nortic countries, report R-189*, pp. 1-8, 2008.

[7] H. Dillon, A. Emery and A. Mescher, "Benchmark comparison of natural convection in a tall cavity," *Proceedings of the COMSOL Conference 2009 Boston*, 2009.

[8] D. Chenoweth and S. Paolucci, "Natural convection in an enclosed vectical air layer with large horizonal temperature differences," *Journal of Fluid Mechanics*, **vol. 169**, pp. 173-210, 1986.

[9] S. Wakitani, "Flow patterns of natural convection in an air-filled vertical cavity," *Physics of Fluids*, **vol. 10**, **no. 8**, pp. 1924-1928, 1997.

[10] COMSOL, "Buoyance Flow in Free Fluids," *MODEL ID 665*, 2011.

[11] P. Leijendeckers, J. Fortuin, F. Herwijnen and G. Schwippert, Polytechnisch zakboek, A. Huson, 2003, pp. 190, 627.

7. Acknowledgements

The authors of this report are graceful for the support provided by the chair Building Physics from the Department of the Built Environment at the Eindhoven University of Technology which made this work possible. In addition, they want to thank Chris van der Meijden for the experimental results that he provided.